

Bright and photostable single-photon emitter in silicon carbide: supplementary material

BENJAMIN LIENHARD^{1,2,*}, TIM SCHRÖDER¹, SARA MOURADIAN¹, FLORIAN DOLDE¹, TOAN TRONG TRAN³, IGOR AHARONOVICH³, AND DIRK ENGLUND¹

¹Department of Electrical Engineering and Computer Science, Massachusetts Institute of Technology, Cambridge, MA 02139, USA

²Department of Information Technology and Electrical Engineering, ETH Zürich, Gloriastrasse 35, CH-8092 Zürich, Switzerland

³School of Mathematical and Physical Sciences, University of Technology Sydney, Ultimo, NSW 2007, Australia

*Corresponding author: blienhar@mit.edu

Published 13 July 2016

This document provides supplementary information to “Bright and photostable single-photon emitter silicon carbide,” <http://dx.doi.org/10.1364/optica.3.000768>. This supplement consists of additional description of methods, calculations, and data. © 2016 Optical Society of America

<http://dx.doi.org/10.1364/optica.3.000768.s001>

1. RAMAN MODES

For an excitation wavelength of 532 nm, the transverse optical (TO) Raman mode occurs at 555.52 nm due to a Raman shift of 796 cm^{-1} . This peak is not visible in the photoluminescence (PL) spectrum in the first figure of the main manuscript as it is blocked by the 560 nm long-pass filter. The longitudinal optical (LO) Raman mode can be seen at 561.04 nm due to a corresponding shift of 973 cm^{-1} [1].

Low- and room-temperature spectral analysis revealed 4H-SiC specific characteristic peaks in the range of $\sim 579 - 589\text{ nm}$. We assign them to second order Raman effects [2]. The spectral components are visible in S1(a).

2. EMITTER POLARIZATION

The polarization orientation of a linearly polarized laser can be rotated by an arbitrary angle with a half-wave-plate (HWP). The systematic rotation of a HWP, implemented in the excitation beam path, changes the efficiency of the emitter's laser absorption. The change in intensity indicates the absorption polarization orientation of the emitter. The emission polarization can be observed by implementing a HWP in the emission beam path with a subsequent linear polarizer. This general approach to measure the polarization reveals a projection of the emitter polarization orientation on the image plane and is thus centrosymmetric.

A controlled manipulation of the excitation and emission polarization reveals additional information on the out of plane (basal plane) emitter orientation. To calculate the angle between the emitter polarization and the imaging plane, one basic condition needs to be satisfied: the pump laser propagation

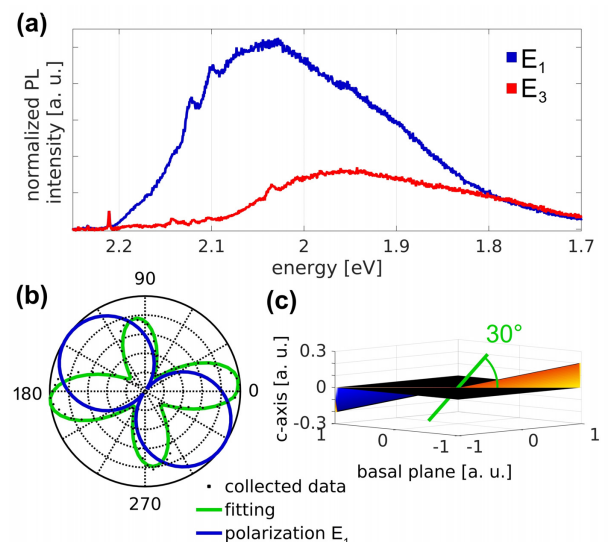


Fig. S1. (a) Spectra from E_1 and E_3 normalized with respect to the LO Raman mode intensity. (b) Polarization measurement and fit according to the method presented in S2. (c) 3 dimensional polarization plot. 30° angle represents the expected vertical orientation of emitters embedded in a hexagonal polytype.

direction is required to deviate from perfect orthogonality (denoted by ϵ) to the HWP front surface. The excitation of the emitter, hence the polarization dependent emission intensity, is

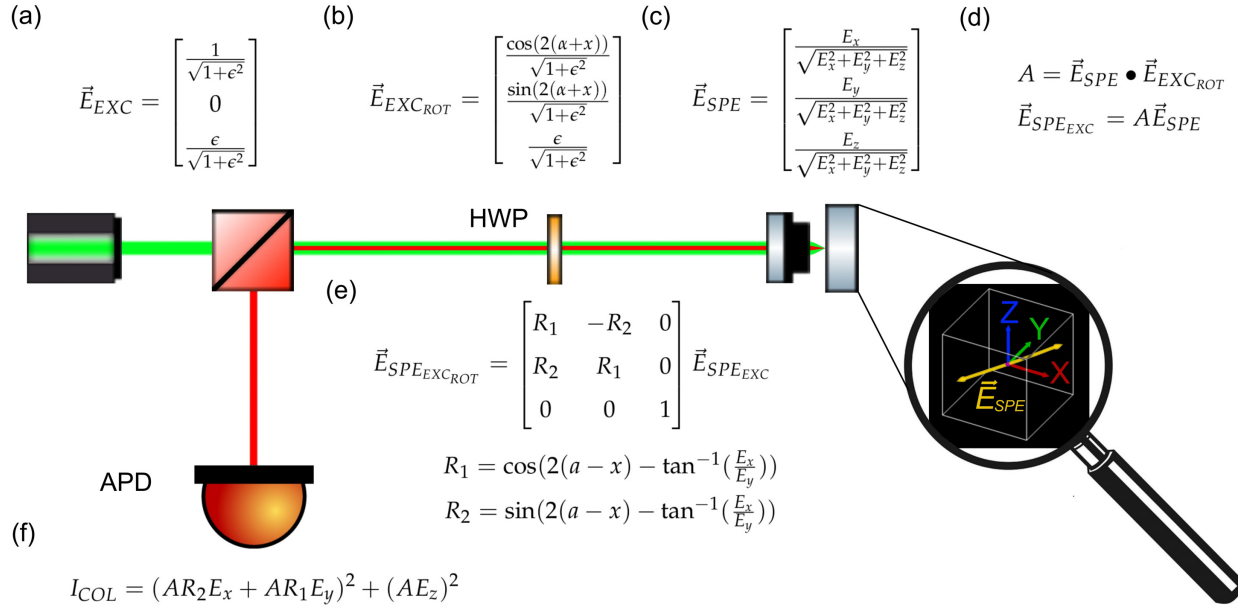


Fig. S2. Setup with a polarized beamsplitter (PBS), half-wave-plate (HWP), objective, and an avalanche photo diode (APD). The vertically linearly polarized laser (a) is step-wise rotated by the HWP (initial angle: α , increment: x) (b) and focused by the objective (c) to excite the emitter. The emitted photons are linearly polarized (d). The emitter's polarization orientation is independent of the excitation laser polarization. The emitted signal is rotated by the HWP (e) and the horizontal polarization fraction is deflected by the PBS and collected by the APD (f).

not centrosymmetric. The resulting bilateral symmetry allows a relative differentiation between separate emitters and their out of plane orientation.

Fig. S2 illustrates graphically and mathematically the process of polarization dependent excitation, emission, and collection. The vertically linearly polarized excitation laser is described as a normalized vector with a small amplitude in the direction of propagation (z-component). The HWP (fast axes at angle α , relative to vertical axis) rotates the polarization of the excitation laser by increments of x . The emitter polarization orientation is modeled as a normalized vector with components E_x , E_y , and E_z . An orthogonal projection (dot product) of the rotated excitation laser vector ($\vec{E}_{EXC_{ROT}}$) on the emitter (\vec{E}_{SPE}) yields an emission intensity amplitude and orientation parallel to the emitter polarization orientation. The HWP rotates the emission polarization whereon the horizontal polarization component of the emission is separated from the excitation beam path and collected by one APD.

Applying this mathematical approach on the emitter reveals an angle of $10 \pm 3^\circ$ between the optimal emitter excitation and the basal plane, illustrated in Fig. S1.

3. 3-LEVEL SYSTEM

Second-order autocorrelation histograms, $g^{(2)}(\tau)$, allow an estimation of the number and nature of addressable states of the underlying quantum system. The histogram is an overview of the probability of detecting a photon under the condition that already one photon was detected at $\tau = 0$ because of a direct or indirect decay from the excited state (probability of populated excited state at time τ : $p_e(\tau)$) to the ground state. This conditional probability can be mathematically described by $g^{(2)}(\tau) = \lim_{t \rightarrow \infty} p_e(\tau)/p_e(t)$ and the initial condition

($p_g(0) = 1$) [3–5]. The normalization term $\lim_{t \rightarrow \infty} p_e(t)$ represents the asymptotic transition dynamics towards the stationary regime.

τ_1 can be described as a 2-level system represented by the sum of the transition rates of an electron between the ground and excited state. Eq. S1(a) is a linear approximation by substituting γ_{ge} by ($aP_{opt}\gamma_{eg}$), described in Eq. S1(b), with a as a fitting parameter to accommodate the optical excitation power (P_{opt}) combined with γ_{eg} to γ_{ge} . Therefore, if there is no optical excitation power ($P_{opt} = 0$), τ_1 can be interpreted as the lifetime of the excited state [3, 5].

$$\frac{1}{\tau_1} = \gamma_{ge} + \gamma_{eg}, \quad (\text{S1a})$$

$$\frac{1}{\tau_1} \approx \gamma_{eg}(1 + aP_{opt}). \quad (\text{S1b})$$

Eq. S2(a) describes the behavior of the metastable state by a sum of the transition rates from the excited to the metastable state and from the metastable to the ground state. Eq. S2(a) is approximated by Eq. S2(b) by replacing τ_1 with Eq. S1(b).

$$\frac{1}{\tau_2} = \gamma_{mg} + \gamma_{em} \frac{\gamma_{ge}}{\gamma_{ge} + \gamma_{eg}} = \gamma_{mg} + \gamma_{em} \gamma_{ge} \tau_1, \quad (\text{S2a})$$

$$\frac{1}{\tau_2} \approx \gamma_{mg} + \gamma_{em} \frac{\gamma_{ge}}{\gamma_{eg}(1 + aP_{opt})}. \quad (\text{S2b})$$

The remaining fitting parameter of $g^{(2)}(\tau)$ for a 3-level system is α , mathematically described by Eq. S3, accounting for the non-radiative decays. α is a product of the excitation probability of an electron and the subsequent decay to the metastable state.

$$\alpha = \frac{\gamma_{ge}}{\gamma_{ge} + \gamma_{eg}} \frac{\gamma_{em}}{\gamma_{mg}}. \quad (\text{S3})$$

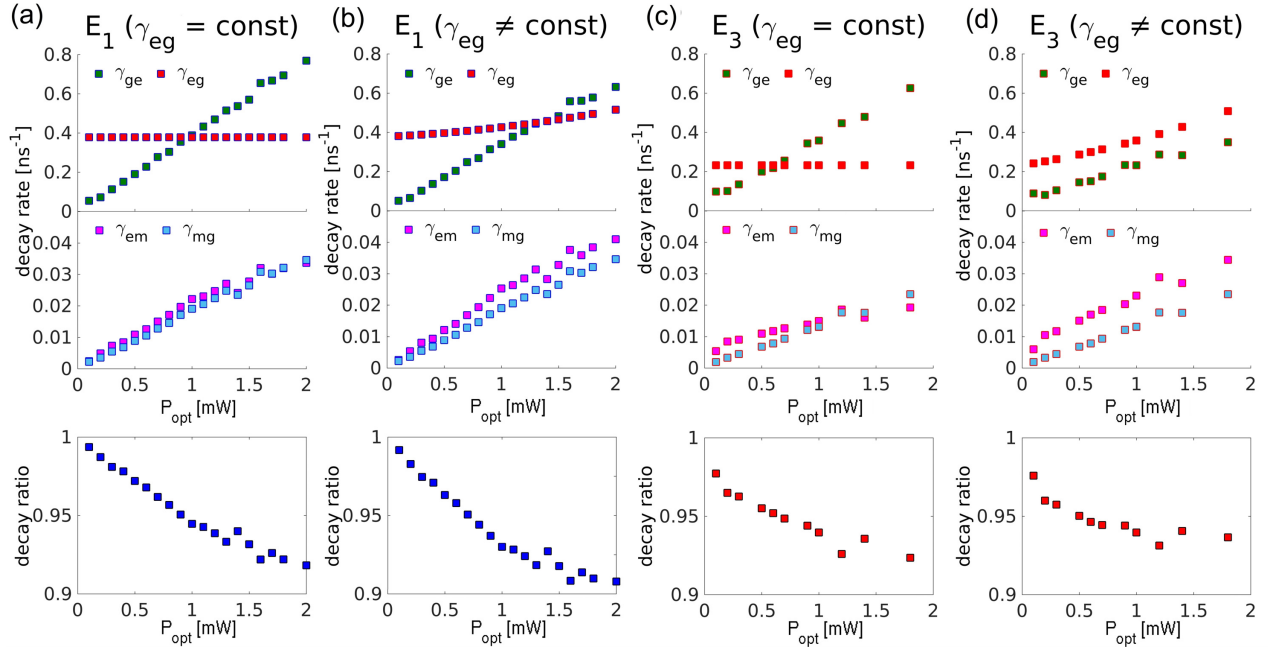


Fig. S3. Decay rates for E_1 and E_3 assuming γ_{eg} as constant (a) and (c) and depending on PL intensity measurement (b) and (d). First graph: transitions between ground and excited state (γ_{ge} , γ_{eg}). Second graph: decays from excited to metastable state and metastable to ground state (γ_{em} , γ_{mg}). Third graph: ratio between decays from the excited state to the ground state (γ_{eg}) relative to all excited state decays ($\gamma_{eg} + \gamma_{em}$) (Eq. S9).

4. RATE EQUATIONS

For a better understanding of the different measurement results we evaluated the decay rates of the emitter states. The four unknown different decay rates of a 3-level system, introduced in Eq. S5, are calculated based on the three fitting parameters of $g^{(2)}(\tau)$ for a 3-level system. The lack of a fourth equation can be resolved by assuming the decay rate from the excited state to the ground state to be power independent, $\gamma_{eg}(P_{opt}) = \text{constant}$. The general power independence of direct decay rates to an energetically lower state serves as main motivation to assume γ_{eg} as constant. The results for emitter E_1 and E_3 are shown in Fig. S3(a) respectively (c).

$$\begin{pmatrix} \dot{p}_g \\ \dot{p}_e \\ \dot{p}_m \end{pmatrix} = \begin{pmatrix} -\gamma_{ge} & \gamma_{eg} & \gamma_{mg} \\ \gamma_{ge} & -\gamma_{eg} - \gamma_{em} & 0 \\ 0 & \gamma_{em} & -\gamma_{mg} \end{pmatrix} \begin{pmatrix} p_g \\ p_e \\ p_m \end{pmatrix}. \quad (\text{S4})$$

$$g^2(\tau) \approx 1 - (1 + \alpha) \exp\left(-\frac{\tau}{\tau_1}\right) + \alpha \exp\left(-\frac{\tau}{\tau_2}\right). \quad (\text{S5})$$

E_1 illustrated in Fig. S3(a) reveals a higher absorption rate, γ_{ge} , and faster decay rates with increasing excitation power compared to E_3 , represented in Fig. S3(c). This result agrees with the measured PL intensities of E_1 relative to E_3 .

$$\gamma_{ge} = \frac{1}{\tau_1} - \gamma_{eg}, \quad (\text{S6a})$$

$$\gamma_{mg} = \frac{1}{(\alpha + 1)\tau_2}, \quad (\text{S6b})$$

$$\gamma_{em} = \frac{\alpha}{(\alpha + 1)\tau_2(1 - \gamma_{eg}\tau_1)}. \quad (\text{S6c})$$

To keep the system dynamic as a whole, a fourth input parameter can be deduced from the PL intensity measurements [4]. All the dynamic decay rates are contained in Fig. S3(b) respectively (d).

$$R_{COL}(P_{opt}) = \frac{R_{INF}P_{opt}}{P_{SAT} + P_{opt}} + a_{BG}P_{opt} + a_D. \quad (\text{S7})$$

$$R_{INF} = \gamma_{eg} \left(1 + \frac{\gamma_{em}}{\gamma_{mg}}\right)^{-1}, \quad (\text{S8a})$$

$$P_{SAT} = R_{INF} \left(1 + \frac{\gamma_{em}}{\gamma_{eg}}\right) \frac{\hbar\omega}{\sigma} = \frac{R_{INF}}{Q} \frac{\hbar\omega}{\sigma}. \quad (\text{S8b})$$

Eq. S7, introduced in the main manuscript, is composed of Eq. S8(a,b). Eq. S8(a) describes the saturated count rate at infinite power which depends on all radiative decays, γ_{eg} , weighted by the ratio of the metastable state lifetime, γ_{mg} , and the total decay time from the excited state via the metastable state to the ground state, $\gamma_{em} + \gamma_{mg}$. Eq. S8(b), the saturation power, is composed of two components. The first component is P_{SAT} , which is the power at which half the saturated count rate is detected, directly depends on the saturation count rate at infinite power, R_{INF} , normalized by the probability of radiative decays, described by Eq. S9. Furthermore, the saturation power is composed of the energy per pump photon ($E = \hbar\omega$) and the absorption cross section (σ).

Eq. S7 with the initial condition of $\gamma_{eg} = 1/\tau_1$ with no optical excitation power, $P_{opt} = 0$, allows to fit γ_{eg} for $P_{opt} > 0$ to the measured power dependent PL intensities for a constant collection efficiency, η_{COL} . We calculated a total collection efficiency for our setup of $0.14 \pm 0.02\%$. Fig. S3(b) and (d) illustrate the results for E_1 and E_3 .

A comparison between Fig. S3(a) and (b), E_1 , reveals that the approximation of a constant γ_{eg} is sufficient. However a comparison between Fig. S3(c) and (d), E_3 , indicates a change of the transition rates between ground and excited state.

The ratio between decays from the excited state to the ground state compared to all first order decays from the excited state, defined here as decay ratio, is calculated with Eq. S9. The third row of Fig. S3(a-d) shows the power dependent evolution of decay ratios for E_1 and E_3 . The saturating decay ratio is indicating a highly efficient single photon emitter with more than 90 % radiative decay efficiency.

$$Q = \frac{\gamma_{eg}}{\gamma_{eg} + \gamma_{em}}. \quad (\text{S9})$$

The decay rates from the excited state to the metastable state, second row of Fig. S3, are constant for ideal 3-level models. The slightly power dependent transitions to and from the metastable state reveal additional energy levels. However, the good agreement with a 3-level system and the dominance of γ_{eg} relative to γ_{em} (9:1) indicates that transitions to higher order levels must be of even smaller probability and can therefore be neglected.

5. 3C-SiC

3C-SiC is next to 4H-SiC and 6H-SiC one of the most common polytypes in SiC. Fig. S4 illustrates the crystal structure of 3C-SiC with a diatomic primitive base and a face centered cubic Bravais lattice. The basal plane, shown in Fig. S4(b) indicates the orthogonality between covalent bonds. The perpendicular bonds in the basal plane could explain the two different orthogonal polarization states.

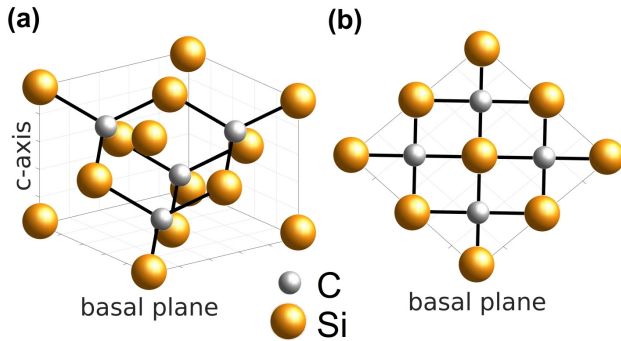


Fig. S4. (a) 3C-SiC with zincblende structure containing carbon (C) and silicon (Si) atoms. (b) View along c-axis on top of basal plane. Bonds form an orthogonal grid.

REFERENCES

1. D. W. Feldman, "Phonon dispersion curves by raman scattering in SiC, polytypes 3c, 4h, 6h, 15r, and 21r," *Physical Review* **173** (1968).
2. J. C. Burton, L. Sun, F. H. Long, Z. C. Feng, and I. T. Ferguson, "First- and second-order raman scattering from semi-insulating 4H-SiC," *Physical Review B* **59**, 7282 (1999).
3. S. C. Kitson, P. Jonsson, J. G. Rarity, and P. R. Tapster, "Intensity fluctuation spectroscopy of small numbers of dye molecules in a microcavity," *Physical Review A* **58**, 620 (1998).
4. M. Berthel, O. Mollet, G. Dantelle, T. Gacoin, S. Huant, and A. Drezet, "Photophysics of single nitrogen-vacancy centers in diamond nanocrystals," *Physical Review B* **91**, 035308 (2015).
5. I. Aharonovich, "Chromium single-photon emitters in diamond fabricated by ion implantation," *Physical Review B* **81** (2010).